

# UC San Diego

## UC San Diego Previously Published Works

### Title

Centrifuge Modeling of End-Restraint Effects in Energy Foundations

### Permalink

<https://escholarship.org/uc/item/2h20h4xx>

### Journal

Journal of Geotechnical and Geoenvironmental Engineering, 141(8)

### ISSN

1090-0241

### Authors

Goode, JC  
McCartney, John S

### Publication Date

2015-08-01

### DOI

10.1061/(asce)gt.1943-5606.0001333

Peer reviewed

# CENTRIFUGE MODELING OF END-RESTRAINT EFFECTS IN ENERGY FOUNDATIONS

By J.C. Goode III, M.S., S.M.ASCE<sup>1</sup> and John S. McCartney, Ph.D., P.E., M.ASCE<sup>2</sup>

**Abstract:** This study presents the results from physical modeling experiments on centrifuge-scale energy foundations in dry sand and unsaturated silt layers. These experiments were performed to characterize end restraint effects on soil-structure interaction for energy foundations in different soils, and include tests on foundations with semi-floating and end-bearing toe boundary conditions and free- and restrained-expansion head boundary conditions. Two scale-model energy foundations having different lengths were constructed from reinforced concrete to simulate end-bearing and semi-floating conditions in soil layers having the same thickness. The foundations include embedded thermocouples and strain gages, which were calibrated under applied mechanical loads and nonisothermal conditions before testing. The variables measured during the experiments include axial strain and temperature distributions in the foundation, temperature and volumetric water content measurements in the soil, vertical displacements of the foundation head and soil surface, and axial stress at the foundation head. These variables were used to calculate the distributions in thermal axial stress and thermal axial displacement, which are useful in evaluating soil-structure interaction mechanisms. The results confirm observations from full-scale energy foundations in the field for end-bearing foundations, and provide new insight into the behavior of semi-floating foundations. Heating of the semi-floating foundations in compacted silt led to a clear increase in ultimate capacity, potentially due to changes in radial normal stress and thermally-induced water flow, while heating of the semi-floating foundations in dry sand led to a negligible change in ultimate capacity.

---

<sup>1</sup> Engineer, Shannon and Wilson, Denver, CO

<sup>2</sup> Associate Professor, Department of Structural Engineering, University of California San Diego, 9500 Gilman Dr. La Jolla, CA 92093-0085

## 23 INTRODUCTION

24 The effects of incorporating geothermal heat exchangers into subsurface infrastructure is an  
25 emerging topic in geotechnical engineering. In particular, the incorporation of heat exchangers  
26 into drilled shaft foundations has been shown to provide a sustainable approach to transfer  
27 thermal energy to and from the ground for a lower installation cost than traditional borehole-type  
28 geothermal heat exchangers (Brandl 1998; Brandl 2006). Observations from several case  
29 histories involving full-scale energy foundations indicate that heating and cooling will lead to  
30 movements associated with thermal expansion and contraction of the foundation element and  
31 surrounding soil (Laloui et al. 2003; Brandl 2006; Laloui et al. 2006; Bourne-Webb et al. 2009;  
32 Bouazza et al. 2011; Amatya et al. 2012; McCartney and Murphy 2012; Akrouch et al. 2014;  
33 Murphy et al. 2014; Sutman et al. 2014; Murphy and McCartney 2014; Wang et al. 2014a).  
34 These thermally-induced movements may lead to the generation of axial stresses due to the  
35 restraint of the foundation provided by soil-structure interaction and end-restraint boundary  
36 conditions. Although the role of end-restraint boundary conditions at the head and toe of the  
37 foundation has been assessed qualitatively in some of these studies (Laloui et al. 2006; Amatya  
38 et al. 2012; Murphy et al. 2014), it has not been evaluated thoroughly due to the complexity  
39 associated with understanding these conditions in a full-scale site. The end-restraint boundary  
40 conditions may play an important role in design guidelines which are being proposed for energy  
41 foundations (Suryatriyastuti et al. 2013; Mimouni and Laloui 2014).

42 This study involves the use of physical modeling tests in a geotechnical centrifuge to  
43 evaluate the effects of end-restraint boundary conditions on energy foundations following an  
44 approach introduced by Stewart and McCartney (2014). Stewart and McCartney (2014)  
45 evaluated transient heating and cooling of a centrifuge-scale energy foundation with end-bearing

46 boundary conditions, and showed using a single test how instrumentation could be used to assess  
47 soil-structure interaction mechanisms. The results from their centrifuge tests and those from  
48 following studies (Goode et al. 2014, Goode and McCartney 2014) have been compared with  
49 numerical simulations (Wang et al. 2012, 2014b), with heat transfer being considered in model  
50 scale. Although centrifuge tests represent a comparatively simple situation compared to field  
51 tests, they still provide empirical data that can be used for calibration of parameters or  
52 verification of load transfer analyses (Knellwolf et al. 2011) and finite element analyses (Laloui  
53 et al. 2006; Wang et al. 2012, 2014b; Ouayang et al. 2012).

54 An advantage of physical modeling in the centrifuge over full-scale testing is that the  
55 properties of scale-model foundations and soil layers can be carefully controlled and different  
56 configurations can be considered for lower costs. Centrifuge modeling also permits incorporation  
57 of dense instrumentation arrays to capture thermo-mechanical effects in the energy foundation as  
58 well as thermo-hydro-mechanical effects in the surrounding soil, both of which are necessary to  
59 validate predictions from finite element analyses. Another advantage of centrifuge modeling is  
60 that scale-model energy foundations can be loaded to failure to destructively characterize the  
61 effects of temperature on the load-settlement curve and the associated ultimate side shear  
62 resistance and end bearing (McCartney and Rosenberg 2011).

63 The objective of this study is to present the results from a series of centrifuge modeling  
64 experiments to quantify the role of end restraint boundary conditions at the foundation head and  
65 toe in dry sand and unsaturated silt. The approach described by Stewart and McCartney (2013) to  
66 consider the centrifuge scaling conflict between geometric similitude and heat flow is used in  
67 this study. Specifically, the tests in this study were performed by bringing a scale-model energy  
68 foundation to a target temperature, then performing different loading tests. In this case, the

69 results are expected to represent a worst-case scenario, as heat flow in the centrifuge model will  
70 have affected a greater zone of soil than that affected by a prototype foundation in the field  
71 heated for the same scaled time. Nonetheless, the relatively stiff silt and dry sand evaluated in  
72 this study will not be as significantly affected by temperature changes as soft clays would, so this  
73 worst-case scenario is not expected to differ significantly from a heating test on a full-scale  
74 energy foundation in these soil profiles. A discussion on the calculation of thermal axial stresses  
75 and thermal axial displacements from measured values of thermal axial strain is presented in  
76 Stewart and McCartney (2014) and Murphy et al. (2014), so these calculations are not presented  
77 again in this paper for the sake of brevity. This paper uses the same sign conventions as these  
78 previous studies, where positive values of thermal axial strain and stress denote compression,  
79 and positive displacements denote downward movement.

## 80 **BACKGROUND**

81 Several field studies have evaluated the distributions in thermal axial strain and stress in full-  
82 scale energy foundations. Laloui et al. (2003, 2006) observed increases in thermal axial stress  
83 with depth during heating tests on a 25 m-long energy foundation installed in an  
84 overconsolidated soil deposit after different stories of a building were constructed. The head of  
85 the foundation in a test performed before building construction heaved upward by 4.2 mm  
86 (i.e., -4.2mm displacement) during heating to 21 °C. Bourne-Webb et al. (2009) and Amatya et  
87 al. (2012) also observed an increase in compressive forces during heating of a 23 m-long energy  
88 foundation installed in a layered clay deposit loaded axially from the surface using a load frame.  
89 They used fiber optic sensors to measure a continuous distribution in thermal axial strain with  
90 depth, and observed tensile thermal axial stresses at the toe of the foundation during cooling.  
91 Bouazza et al. (2011) and Wang et al. (2014a) used a pair of Osterberg cells embedded in an

92 energy foundation to translate a section of the shaft upward and downward to characterize  
93 changes in side shear resistance with temperature. McCartney and Murphy (2012) and Murphy  
94 and McCartney (2014) evaluated the stresses and strains in a pair of 12.7 m-long energy  
95 foundations beneath an 8-story building during typical heat pump operations, and observed both  
96 the greatest compressive and tensile thermal axial stresses near the toe of the foundation during  
97 heating and cooling, respectively. Murphy et al. (2014) characterized soil structure interaction  
98 mechanisms including distributions in thermal axial stress, strain, displacement and mobilized  
99 side shear for three end-bearing foundations in a sandstone deposit. They observed that  
100 differences in head restraint provided by the overlying building had an effect on the magnitude  
101 of thermally-induced stresses and displacements.

102 Bourne-Webb et al. (2009) proposed hypothetical representations of the mechanisms of  
103 thermo-mechanical soil-structure interaction in “floating” energy foundations that have no end  
104 bearing, and Amatya et al. (2012) extended these representations to cases with non-zero end-  
105 bearing (semi-floating and end-bearing conditions). A floating foundation is expected to expand  
106 about its center during uniform heating, an end-bearing foundation is expected to expand upward  
107 from the base, and a semi-floating foundation is expected to have an intermediate response.  
108 Knellwolf et al. (2011) referred to the point of zero thermal axial displacement about which the  
109 foundation expands during heating as the null point, and noted that this is an important parameter  
110 in thermo-mechanical soil-structure interaction analyses. The null point is typically near the toe  
111 of the foundation for end-bearing energy foundations (Stewart and McCartney 2013; Murphy et  
112 al. 2014). Although the location of the null point for semi-floating foundations is expected to be  
113 near the center of the foundation, the behavior of these foundations in the field hasn’t been well  
114 characterized. The hypothetical representations of soil-structure interaction mechanisms of

115 Bourne-Webb et al. (2009) and Amatya et al. (2012) are useful when evaluating field  
116 measurements and simulation results, especially when differentiating the effects of temperature  
117 from those of mechanical loading on the distributions in axial stress and side shear resistance.

## 118 **MATERIALS**

### 119 **Nevada Sand**

120 Six of the tests in this study were performed on energy foundations in a layer of dry Nevada  
121 sand having a relative density of 60% (void ratio of 0.75). The sand consists of uniform angular  
122 particles, and based on the characteristic grain size values shown in Table 1 has a Unified Soil  
123 Classification System (USCS) classification of SP (poorly graded sand). At a relative density of  
124 60% and a mean stress of 100 kPa, Nevada sand has a friction angle of 35°, a shear modulus of  
125 30 MPa, and a Poisson's ratio of 0.3. The thermal conductivity measured using a KD2Pro  
126 thermal needle from Decagon Devices of Pullman, WA was 0.265 W/mK. The sand layers were  
127 prepared using air pluviation around the energy foundation.

### 128 **Bonny Silt**

129 Four of the tests in this study were performed on energy foundations installed in a layer of  
130 Bonny silt, which is the same soil used by Stewart and McCartney (2013). Relevant geotechnical  
131 properties of Bonny silt are also summarized in Table 1. The liquid and plastic limits are 26 and  
132 24 and the fines content is 84%, so Bonny silt has a USCS classification of ML (inorganic silt).  
133 The silt has a specific gravity  $G_s$  of 2.6. The silt layer was prepared using compaction to permit  
134 fast model preparation times and to reach uniform distributions in dry unit weight and water  
135 content with height at the beginning of the tests. The soil layers were prepared by compacting silt  
136 having a gravimetric water content of 14.2% in 76.2 mm-thick lifts around the foundation to  
137 reach a target dry density of 1565 kg/m<sup>3</sup>. A rubber mallet was used to compact the soil around

138 the foundation in 75 mm-thick lifts. The centrifuge test was performed on the soil layer in as-  
139 compacted (unsaturated) conditions. The thermal conductivity of the silt under these compaction  
140 conditions was 1.20 W/mK.

### 141 **Scale-Model Energy Foundations**

142 Two scale-model energy foundation having a diameter of 63.5 mm were fabricated for this  
143 study. One of the foundations has a length of 342.9 mm (short foundation), while the other has a  
144 length of 533.4 mm (long foundation). A centrifuge acceleration of 24g was used in all of the  
145 tests, so the corresponding prototype-scale short and long foundations have a diameter of 1.5 m  
146 and lengths of 8.2 m and 12.7 m, respectively. The foundation diameter is greater than that of  
147 Stewart and McCartney (2014) to provide more space around embedded instrumentation.  
148 Schematics of the foundations are shown in Figure 1.

149 Although drilled shafts are typically cast-in-place, the model foundations were precast in a  
150 cardboard mold having an inside diameter of 63.5 mm to ensure quality construction considering  
151 the extensive embedded instrumentation. The reinforcing cage was formed from welded steel  
152 hardware cloth that simulates the longitudinal and lateral members of a drilled shaft reinforcing  
153 cage. The cage has 12.7 mm-square openings, with 19 gage wire thickness. The cage diameter is  
154 48.5 mm, leaving a concrete cover of 7.5 mm on the sides and 6.35 mm on the top and bottom.  
155 The cage openings were larger than those of Stewart and McCartney (2014), permitting use of a  
156 concrete mixture consisting of 1:2:1.5:1.5 water:cement:sand:coarse aggregate ratio. This  
157 mixture has a larger coarse aggregate fraction and greater size of coarse aggregates (7 mm max)  
158 than that of Stewart and McCartney (2014), making it closer to the mixture used in drilled shafts.

159 Seven strain gages and thermocouples were embedded within the foundation to characterize  
160 the strain response and temperature distribution within the foundations. The strain gages were



161 model CEA-13-250UW-350 from Vishay Precision Group, and were bonded using M-Bond  
162 AE-15 epoxy to 50.8 mm-long, 12.7 mm-wide, and 1.8 mm-thick steel tabs. The tabs have two  
163 6.1 mm-diameter holes at top and bottom for good interaction with the concrete, and the zinc  
164 plating on the tabs was sanded off to provide a smooth surface. The bonded gages were cured  
165 under pressure for 4 hours at 57.2 °C. A Teflon strip was placed over the cured gage, which was  
166 then covered using a waterproof epoxy (Gagekote #5). Miniature thermocouples (Fine wire type  
167 K Model STC TT K 36 3C from Omega) were attached to the steel tabs next to the strain gages.  
168 The finished steel tabs were attached to the inside of the reinforcing cage using thin wire thread  
169 at the locations in Figure 1. The gages were installed on opposing sides of the reinforcing cage  
170 on an alternating basis because of space constraints with the wiring. In addition to the embedded  
171 instrumentation, three heat exchanger loops were affixed to the inside of the reinforcing cage at  
172 an equal spaced around the circumference of the cage. Perfluoroalkoxy (PFA) tubing with an  
173 inside diameter of 3.175 mm was used for the heat exchange loops. The bottom of the loops were  
174 tied to the cage so that they do not cross through the center of the foundation.

175 After the cage and instrumentation were centered in the form, concrete was placed using a  
176 miniature tremie pipe to ensure uniform concrete placement. The form was placed on a vibrating  
177 table during concrete placement for good concrete flow and for extruding entrapped air. When  
178 the concrete had reached the top of the form, a hex-head bolt was placed in the middle of the  
179 foundation to provide a centering point for mechanical loading of the foundation. The  
180 foundations were cured in a fog room for 14 days, after which 14 more days of curing were  
181 permitted after removing the form.

182 Before construction of the foundations, thermo-mechanical calibration tests were performed  
183 on the assembled strain gages by hanging a 27 kg mass from the steel tabs, then heating them

184 with a hot air gun (fixed at a distance of 300 mm from the gage to avoid overheating). The  
185 results of one of the calibration tests on a gage-tab assembly are shown in Figure 2(a). After  
186 reversing the sign of the gage reading so that compression is defined as positive, the raw gage  
187 readings showed negative strains during application of the tensile force, as expected. However,  
188 heating was observed to lead to a reversal of the trend in strain due to differential thermal  
189 expansion of the gauge, steel tab, and epoxy. To account for this behavior, a thermo-mechanical  
190 correction was applied so that the measurements from the gages would yield strains that are  
191 consistent with the properties of steel (i.e., a Young's modulus of  $E_{\text{steel}} = 200 \text{ GPa}$  and a  
192 coefficient of linear thermal expansion of  $\alpha_{\text{steel}} = -13.0 \mu\text{ε}/^\circ\text{C}$ ), as follows:

$$193 \quad \varepsilon_{\text{tab}} = \chi \varepsilon_{\text{raw}} + \Delta T \beta \quad (1)$$

194 where  $\chi$  and  $\beta$  are mechanical and thermal correction factors, respectively, which were defined  
195 individually for each gage. The values of  $\chi$  ranged from 0.34 to 0.52 and the values of  $\beta$  ranged  
196 from -24.9 to -28.4 (Goode 2013). Although these correction factors differed slightly due to  
197 variability in the assembly of the gages, the same pattern of behavior was observed in each gage.  
198 Repeat tests on each gage revealed the same correction factors.

199 After curing, tests were performed on the foundations to characterize their thermo-  
200 mechanical response. First, the foundation was loaded mechanically in stages in a load frame to  
201 evaluate the Young's modulus of the reinforced concrete, then was heated under free-expansion  
202 conditions to evaluate the coefficient of linear thermal expansion. In these tests, it was observed  
203 that the strains calculated using Equation (1) differed from the global foundation strain inferred  
204 from the head displacement measured using a linearly variable differential transformer (LVDT),  
205 potentially due to embedment and alignment effects in the reinforced concrete. Accordingly, a  
206 second calibration equation was defined for each gage, as follows:

207  $\varepsilon = \mu\varepsilon_{tab} + \Delta T \xi$  (2)

208 where  $\varepsilon$  is the thermo-mechanical strain,  $\mu$  is a mechanical correction factor for embedment  
209 effects, and  $\xi$  is a thermal correction factor for embedment effects.

210 An example of the corrected strain values during mechanical loading of the long foundation  
211 in even increments of axial stress from 281 to 706 kPa is shown in Figure 2(b). Although the  
212 effects of bending are observed in the gages due to the unrestrained length of the relatively  
213 slender foundation, a linear trend in mechanical strains with increasing axial stress is observed. A  
214 multiplicative correction factor of  $\mu = 0.5$  was used for all of the gages to to match the global  
215 strain values for the reinforced concrete calculated from the LVDT measurements, which are  
216 shown at a depth of zero in Figure 2(b). The same mechanical correction factor was used for all  
217 of the gages to avoid covering up the effects of bending observed in the strain profiles. The  
218 global strain values from the LVDT correspond to a Young's modulus of 33 GPa, which is  
219 similar to the value expected for drilled shafts (~30 GPa).

220 The free-expansion heating tests were performed on the foundations by circulating water  
221 having a temperature of 55 °C through the heat exchange tubing when the foundation was  
222 standing vertically on a rigid base (Goode 2013). During the free expansion tests, it was expected  
223 that all of the gages would show the same strain values for a given temperature, as the foundation  
224 was unrestrained. However, there were some slight differences with height that were attributed to  
225 varying distances from the heat exchanger tubing to the gages, differential expansion of the steel  
226 tabs and the surrounding concrete, slight variations in the alignment of the gages, and variations  
227 in the steel tab-concrete interaction (Goode 2013). Accordingly, values of  $\xi$  ranging from 3.8 to  
228 10 were defined so that the gages show the same slope as the global thermal expansion strain  
229 defined from the LVDT displacements, as shown in Figure 2(c). The global strain inferred from

230 the head displacements indicates that the reinforced concrete has a coefficient of thermal  
231 expansion  $\alpha_c$  of  $-16 \mu\epsilon/^\circ\text{C}$  for the short foundation and  $-15 \mu\epsilon/^\circ\text{C}$  for the long foundation. These  
232 values are greater than those expected in drilled shafts due to the greater percentage of heat  
233 exchange tubing in the foundation cross section.

234 Despite the number of different corrections applied to the measured strains, all of the gages  
235 were considered in a systematic manner. The foundations were reused in several different  
236 centrifuge tests in which the gages provided consistent results. Further, after application of the  
237 corrections, the strain values from the gages consistently met several checks during the  
238 centrifuge tests, such as being equal or less than the free expansion strain of the reinforced  
239 concrete during heating. Gages 2 and 6 in the short foundation were damaged during installation,  
240 but all seven gages functioned in the long foundation.

## 241 **EXPERIMENTAL SETUP**

242 Schematics of the container used in this study to evaluate the thermo-mechanical strain  
243 distributions for the energy foundations tested in sand and silt are shown in Figure 3. The  
244 schematics show the case of the semi-floating foundation, but the same configuration was used  
245 for the end-bearing foundation with its toe resting on the bottom of the container. The container  
246 is a cylindrical aluminum tank with an inside diameter of 0.6 m, wall thickness of 13 mm, and a  
247 height of 0.54 m. A 13 mm-thick insulation sheet was wrapped around the container to minimize  
248 heat transfer through the sides of the cylinder. The bottom of the container is not insulated to  
249 provide a stiff platform for loading. The load frame consists of a steel frame mounted atop a  
250 rectangular steel platform resting on the centrifuge basket. A pneumatic piston was used to apply  
251 axial loads to the foundation in load-control conditions, and the applied load was measured using  
252 a load cell. The temperature control system developed by Stewart and McCartney (2014) was

253 used in this study. This system is used to control the temperature of the foundation, rather than to  
254 simulate the heat exchange processes encountered in an energy foundation in the field.

255 The locations of instrumentation incorporated into the centrifuge container are also shown in  
256 Figure 3. Two LVDTs were placed on top of the foundation for redundancy and two others were  
257 placed on the soil surface at different radial distances from the foundation. The LVDTs were  
258 mounted on aluminum bars connected to two support beams connected to the top of the  
259 container. The LVDT readings were corrected to account for the change in the ambient  
260 temperature of the centrifuge chamber. Goode (2013) observed that a stationary LVDT showed a  
261 phantom model-scale settlement of  $0.0246\Delta T_{\text{ambient}}$  (in mm), where  $\Delta T_{\text{ambient}}$  is the change in  
262 temperature of the centrifuge chamber from the beginning of the test. Four thermocouple profile  
263 probes for measuring soil temperature with depth were inserted in the soil layers at different  
264 radial locations from the foundation, and dielectric sensors (model EC-TM from Decagon  
265 Devices) for measurement of volumetric water content and temperature were installed in the  
266 Bonny silt layers. The results from these sensors are not presented here but are reported by  
267 Goode (2013).

## 268 **EXPERIMENTAL PROCEDURES**

269 The same procedures were used for all of the tests on the semi-floating foundations. Seven  
270 tests were performed on the semi-floating foundations in different soil layers, as summarized in  
271 Table 2. After assembly of the container within the load frame on the centrifuge basket, the  
272 centrifuge was spun to a target centripetal acceleration of 24g. After the LVDTs on the  
273 foundations and soil indicated the system was at equilibrium, a prototype-scale axial load of  
274 approximately 360 kN (axial stress of 197 kPa) was applied to the energy foundation. The  
275 foundations were then heated to the target temperatures listed in Table 2 in load-control

276 conditions, which means that the top of the foundation is free to move upward due to thermal  
277 expansion (i.e., negligible head stiffness). After maintaining a constant foundation temperature  
278 for at least 30 minutes, the semi-floating foundation was loaded to approximately 2400 kN then  
279 unloaded. This magnitude of head load led to a prototype-scale head settlement that was  
280 approximately 0.013 to 0.015 times the diameter of the foundations.

281 Three tests were performed with the end-bearing foundation, as summarized in Table 2, each  
282 with different testing procedures. The two tests on the end-bearing foundation in sand involved  
283 an evaluation of the role of head restraint. Test 8 involved a load-control heating test under an  
284 axial load of 1200 kN while Test 9 involved a stiffness control test in which a section of threaded  
285 rod was used to preload the foundation to 1000 kN. These two tests were the only two that were  
286 performed in the same sand layer, albeit on different days to permit the system to cool after the  
287 load-control test. The initial load differed between these two tests as the preloading had to be  
288 performed before spin-up of the centrifuge, and the self-weight of the load cell applied an  
289 additional load during centrifugation. Despite the difference in axial load the role of head  
290 restraint can still be evaluated from these tests. Test 10 on the end-bearing foundation in silt  
291 involved heating of the foundation in load-control conditions in stages. After reaching a steady  
292 temperature at each stage, the foundation was loaded and unloaded. Although this is not expected  
293 to cause failure, the role of heating on the slope of the load-settlement curve can be assessed.

## 294 **EXPERIMENTAL RESULTS**

295 The results from the four tests on the semi-floating foundations in sand (Tests 1-4) are shown  
296 in Figure 4. These tests were originally presented by Goode et al. (2014). The data in these  
297 figures are presented in prototype scale, so the loads and displacement during spin-up of the  
298 centrifuge are not shown. The settlement of the foundation and soil shown in this figure were

299 zeroed at the end-of spin-up and a period of time was permitted for equilibration under the  
300 applied centripetal acceleration. The results in the top row of this figure include the settlement of  
301 the soil surface and foundation head during equilibration and application of the seating load. In  
302 all cases the foundation and soil surface quickly reached equilibrium. The results in the second  
303 row of this figure include the temperatures at different depths of the foundation. In all four tests  
304 the foundation temperature was relatively constant with depth. The temperature control system  
305 did not permit precise control of the temperature and occasionally led to fluctuations in  
306 temperature with time, but the temperatures were within 2-3 °C of the target value. The results in  
307 the bottom row show the axial strains in the foundation. Spin-up and application of the seating  
308 load led to negligible strains in the foundation. During heating of the foundations, negative  
309 strains were measured, signifying expansion. During loading and unloading of the foundation  
310 after reaching the target temperature, a clear increase in strain was measured, denoting a  
311 compressive strain superimposed atop the thermal expansion as expected. The strains due to  
312 heating are greater than those due to mechanical loading, which reflects the importance of  
313 considering thermo-mechanical effects in energy foundations.

314 The results from the three tests on the semi-floating foundation in Bonny silt (Tests 5-7) are  
315 shown in Figure 5. Different from the tests on Nevada sand, the results in the top row of this  
316 figure indicate that the foundation and soil continued to settle under self-weight conditions  
317 throughout the test. However, the effects of heating and subsequent mechanical loading of the  
318 foundation can clearly be observed superimposed atop the gradual settlement. As the foundation  
319 and soil were both settling by the same amount before heating started, it is expected that the  
320 effects of dragdown were not significant. The results in the middle row of the figure also indicate  
321 the foundation temperature was within 3 °C of the target value during mechanical loading.

322 Similar to the tests on Nevada sand, the results in the bottom row of this figure indicate that the  
323 strains due to heating are greater than the strains due to mechanical loading despite the different  
324 soil type. Although the bottom strain gage shows an inconsistent tensile strain during mechanical  
325 loading in Tests 5 and 6, the change in strain during heating is consistent with the strains in the  
326 rest of the foundation.

327 The results from the two tests on the end-bearing foundation in Nevada sand (Tests 8 and 9)  
328 are shown in Figure 6. These tests were originally presented by Goode and McCartney (2014).  
329 Although the settlement results in the top row of this figure indicate that the soil appears not to  
330 have reached equilibrium before mechanical loading, the scale of displacement is much smaller  
331 than that shown in Figure 4 and it can be considered to be constant. The results in Figure 6(a)  
332 clearly show the downward settlement of the foundation head during application of the  
333 foundation load, while the results in Figure 6(b) show a negligible settlement of the foundation  
334 head after spin-up of the centrifuge. The results in Figures 6(c) and 6(d) indicate that the  
335 temperatures at different depths in the foundation were relatively similar except at the bottom.  
336 This occurred because the bottom of the container was not insulated. The results in Figure 6(e)  
337 indicate that the positive compressive strains were greatest at the top of the foundation during  
338 application of the axial load as expected, while the strains in the foundation tested under stiffness  
339 control shown in Figure 6(f) were inconsistent during spin-up and equilibration. During heating,  
340 the strains in both tests mimicked the trend in the temperature of the foundations.

341 The results of the end-bearing foundation tested in the silt layer (Test 10) are shown in  
342 Figure 7. Similar to the tests on the semi-floating foundation in silt, the soil surface gradually  
343 settled throughout the test as shown in Figure 7(a). The foundation showed a relatively large,  
344 irrecoverable settlement during the initial loading test at room temperature. The irrecoverable



345 displacement on the first cycle may have been due to seating of the toe of the foundation on the  
346 bottom of the container. During heating, the foundation was observed to heave upward as  
347 expected. The amount of head movement upon each loading test is similar during the subsequent  
348 cycles. The temperatures of the foundation shown in Figure 7(b) show that the target temperature  
349 was initially overshoot in each of the heating stages, but eventually stabilized at the target values.  
350 The axial strains shown in Figure 7(c) clearly show the effects of loading and heating of the  
351 foundation, with greater effects observed due to heating.

## 352 **ANALYSIS OF RESULTS**

### 353 **Effect of Soil Type on Soil-Structure Interaction in Semi-Floating Foundations**

354 Profiles of different variables relevant to the evaluation of soil-structure interaction  
355 mechanisms in the semi-floating foundations in sand and silt layers are shown in Figures 8 and 9,  
356 respectively. The temperature distributions in the semi-floating foundations in sand and silt are  
357 shown in Figures 8(a) and 9(b), respectively, for different average changes in temperature of the  
358 foundations. These profiles were obtained at instances in time in Tests 2-4 and 6 and 7 at which  
359 the foundation had reached a stable temperature, but before mechanical loading of the  
360 foundation. In both soil layers, the temperatures were relatively constant with depth (within  $\pm 1.5$   
361  $^{\circ}\text{C}$  of the average value).

362 For these same instances in time, the thermal axial strains in the foundations are shown in  
363 Figures 8(b) and 9(b) for the foundations in sand and silt, respectively. The thermal axial strains  
364 were defined by zeroing the axial strains shown in Figures 4 and 5 at the beginning of heating.  
365 The thermal axial strains at a depth of zero shown in these figures were not measured using the  
366 strain gages. Instead, they correspond to the theoretical thermal axial strain of the foundation at  
367 free expansion corresponding to the average change in temperature of the foundation

368 ( $\epsilon_{T,free} = \alpha\Delta T_{average}$ ). Thermal axial strains corresponding to free-expansion conditions are  
369 expected at the foundation head in these tests as they were performed under load-control  
370 conditions with negligible head restraint. The thermal axial strains at different depths in the  
371 foundations in both soil layers are relatively close to the free expansion conditions, although the  
372 foundation in silt shows greater (less negative) strains at the middle of the foundation during  
373 both tests at elevated temperatures. The distribution in thermal axial strain is much less  
374 pronounced with depth than that measured by Stewart and McCartney (2014), possibly due to the  
375 greater coefficient of thermal expansion and the greater stiffness of the foundations in this study.

376 The profiles of thermal axial stress are shown in Figures 8(c) and 9(c) for the foundations in  
377 sand and silt, respectively. The thermal axial stresses are equal to the Young's modulus  
378 multiplied by the difference between the measured thermal axial strain and the thermal axial  
379 strain corresponding to free expansion. In both soils, the thermal axial stresses are greatest at the  
380 center of the foundations although the middle gage shows an inconsistent behavior at high  
381 temperatures. The thermal axial stresses at the toe of the foundation are greater than those at the  
382 head, which for no head restraint is zero. Greater thermal axial stresses were observed in the  
383 foundations in silt than the foundations in sand, potentially due to greater soil structure  
384 interaction associated with the effects of compaction.

385 The thermal axial displacements shown in Figures 8(d) and 9(d) for the foundations in sand  
386 and silt, respectively, were obtained by integrating the thermal axial strains with depth and  
387 subtracting these values from the head displacements measured using the LVDT (shown as the  
388 thermal axial displacement at a depth of 0). The slope of the displacement profile reflects the  
389 relative movement between the foundation and the soil during changes in temperature, while the  
390 point where the displacement profile crosses the origin corresponds to the null point. In all

391 cases, the slopes of the displacement profiles were observed to flatten with an increase in the  
392 change of temperature, reflecting greater displacements throughout the foundations with greater  
393 temperatures. However, the trends in the location of the null point observed in Figures 8(d) and  
394 9(d) is inconsistent among the different tests, and is within the accuracy of the LVDT  
395 measurements of the head displacement. For the foundations in sand [Figure 8(d)], a slight  
396 downward movement was observed in the location of the null point for the foundations having a  
397 change in temperature of 7 and 12 °C, while a more significant upward movement was observed  
398 for the foundation with the largest change in temperature of 18 °C. For the foundations in silt  
399 [Figure 9(d)], a slight upward movement in the null point was observed for the test with a greater  
400 change in temperature. It is expected that the downward movement of the toe of the foundation  
401 during heating will mobilize end bearing resistance, leading to a stiffening response at the toe.  
402 Mimouni and Laloui (2014) evaluated energy foundations with a constant head stiffness, and  
403 found that the null point should move downward in response to an increase in restraint near the  
404 toe of the foundation with an increase in the change in temperature, albeit by a relatively small  
405 amount. The upward movement of the null point for the foundations in silt may possibly be  
406 associated with a stiffening of the soil near the head of the foundation due to greater thermally  
407 induced water flow in the soil in this region, which is a subject for further study. Overall, the  
408 trends in the data indicate that movement of the null point for semi-floating foundations may  
409 occur, but the magnitude of movement is expected to be minor. .

#### 410 **Effect of Soil Type on the Ultimate Capacity of Semi-Floating Foundations**

411 The load settlement curves measured for Tests 1-4 and 5-7 are shown in Figures 10(a) and  
412 10(b) for the semi-floating foundations in sand and silt, respectively. These curves were defined  
413 by zeroing the axial displacement and axial load at the beginning of mechanical loading. The

414 foundations in all of the tests nearly reached a settlement corresponding to Davisson's criterion  
415 (Davisson 1973) before reaching the capacity of the pneumatic piston. The load-settlement  
416 curves for sand shown in Figure 10(a) are similar for all four average foundation temperatures,  
417 indicating a negligible effect of temperature on the load-settlement curve. However, the load-  
418 settlement curves for silt in Figure 10(b) show a similar increase in ultimate capacity with  
419 increasing temperature as that observed by McCartney and Rosenberg (2011). The difference in  
420 load-settlement behavior for the semi-floating foundations in sand and silt could be due to the  
421 comparatively low radial resistance provided by the sand compared to the compacted silt. The  
422 lateral stresses in the silt layer are initially much higher due to the compaction process than in the  
423 pluviated sand layer. Although Olgun et al. (2014) indicates that the amount of differential radial  
424 expansion of the foundation may not lead to significant changes in radial stress, the lateral  
425 stresses induced by compaction may have been sufficient to lead to a change in radial stress.  
426 Another possibility is that thermally-induced water flow may have affected the load-settlement  
427 curve of the foundations in Bonny silt as observed by Stewart and McCartney (2014). Although  
428 the two foundations tested at elevated temperatures were heated for similar durations before  
429 loading to failure, the greater temperature may have led to more drying of the soil around the  
430 foundation. This would lead to an increase in effective stress at the interface. This possibility  
431 reflects the importance of performing coupled flow-deformation modeling when energy  
432 foundations are used in unsaturated soils (Wang et al. 2014).

### 433 **Effect of Head Restraint on Soil-Structure Interaction in End-Bearing Foundations**

434 Profiles of different variables relevant to the evaluation of soil-structure interaction  
435 mechanisms in the end-bearing foundations in sand and silt layers are shown in Figures 11 and  
436 12, respectively. The results in Figures 11(a) and 12(a) show the temperature distribution in the

437 end-bearing foundations in sand and silt, respectively, for different average changes in  
438 temperature of the foundations. The profiles in Figure 11(a) correspond to the conditions near the  
439 end of heating, while those in Figure 12(a) correspond to the equilibrium conditions before (open  
440 symbols) and after (closed symbols) mechanical loading at each of the heating stages. The top  
441 and bottom of the foundations were slightly cooler than the center of the foundations, but the  
442 temperatures were relatively constant with depth within the foundations.

443 For these same instances in time, the thermal axial strains in the foundations are shown in  
444 Figures 11(b) and 12(b) for the end-bearing foundations in sand and silt, respectively. The  
445 thermal axial strains at a depth of zero for the foundation tested under load-control conditions in  
446 Figure 11(b) were not measured by the strain gages, but instead correspond to the theoretical  
447 thermal axial strain corresponding to free-expansion conditions. The strain at the foundation  
448 head is not known for the foundation tested under stiffness control conditions. Similar to the  
449 semi-floating foundation, the strains in the foundations in both soil layers are relatively close to  
450 the free expansion conditions. This is in contrast to the results presented by Stewart and  
451 McCartney (2014), possibly due to the much higher coefficient of thermal expansion of the  
452 reinforced concrete evaluated in this study. The thermal axial strain profiles in Figures 11(b) and  
453 12(b) indicate that there is likely a slight bending strain induced in the end-bearing foundations  
454 due to off-axis loading. Although purely axial loading is difficult to control in the centrifuge for  
455 a precast concrete foundation, the effects of temperature can still be observed as a shift to smaller  
456 (more negative) thermal axial strains with heating. The points in these profiles are connected  
457 together with lines to better identify each data set, but in reality they encompass an envelope of  
458 strains on either side of the foundation.

459 The profiles of thermal axial stress are shown in Figures 11(c) and 12(c) for the foundations  
460 in sand and silt, respectively. In both soils, the thermal axial stress profiles are not as simple to  
461 interpret as those in the semi-floating foundation. Stewart and McCartney (2014) observed the  
462 greatest thermal axial stress at the bottom of the energy foundation. However, the shape of the  
463 profiles of thermal axial stress in the end-bearing foundations tested in this study is affected by  
464 the lower temperatures at the head and toe of the foundations, and cannot be directly compared  
465 with the hypothetical curves of Amatya et al. (2014) who assumed a constant temperature with  
466 depth. Nonetheless, this feature can be accounted for in simulations by using the temperature  
467 boundary conditions in the model (Goode 2013). The results in Figure 11(c) indicate that the  
468 foundation heated in stiffness-control conditions has greater stresses near the foundation head  
469 than the foundation heated in load-control conditions. Although more significant bending is  
470 observed in the results in Figure 12(c), the average trend in the data can be observed as the gages  
471 are on opposing sides of the foundation. The axial stress clearly increases during application of  
472 the mechanical load during each of the temperature stages. Similar to the semi-floating  
473 foundation tests, the magnitude of thermal axial stresses were greater in the silt layer than in the  
474 sand layers due to greater soil-structure interaction associated with higher initial radial stresses.

475 The profiles of thermal axial displacements shown in Figures 11(d) and 12(d) for the end-  
476 bearing foundations in sand and silt, respectively, were obtained by integrating the thermal axial  
477 strains with depth and assuming that the displacement at the bottom of the foundation is zero.  
478 Although this assumption implies that the null point is at the base of the foundation, this may not  
479 be the case for energy foundations bearing on more deformable geomaterials. The head  
480 displacement measured using the LVDTs at the surface are shown for verification purposes in  
481 Figure 11(d), and these values correspond very well with those obtained from the thermal axial

482 strains. The results in Figure 12(d) indicate that the thermal axial displacements in the end-  
483 bearing foundation in silt decreased during mechanical loading of the foundation as expected.

#### 484 **Effect of Heating on the Load-Settlement Behavior of End-Bearing Foundations**

485 The head displacement versus temperature of the end-bearing foundations in sand are shown  
486 in Figure 13(a), along with the change in axial load as a function of temperature. As expected,  
487 the load does not change with temperature for the load-control test, but the load increases with  
488 temperature corresponding to a stiffness of 113 kN/m in the stiffness-control test. The end-  
489 bearing foundation in the stiffness-control test shows slightly less head displacement than the  
490 foundation in the displacement-control test, although the difference is not significant.  
491 Nonetheless, this small difference in head displacement corresponded to an increase in axial  
492 stress at the head of the foundation of 100% as shown in Figure 11(c). More research using load-  
493 transfer analyses such as that of Knellwolf et al. (2011) are required to identify the range of head  
494 stiffness values encountered in the field to evaluate the full implications of head restraint.

495 The load-settlement curves for the end-bearing foundation in silt are shown in Figure 13(b).  
496 As mentioned in the discussion of the LVDT data in Figure 7(a), the initial loading stage led to a  
497 large, irrecoverable settlement. However, during each subsequent heating stage the slopes of the  
498 load-settlement curves were relatively consistent after each loading-unloading cycle. This either  
499 indicates that the temperature change does not have a significant impact on the side-shear stress  
500 distribution, which may have an impact on the slope of the load-settlement curve, or that the side  
501 shear stress was fully mobilized during the first loading cycle. The curves are also observed to  
502 shift upward with each temperature stage due to the effects of thermal expansion.

503 **CONCLUSIONS**

504 The impact of end restraint boundary conditions on the distributions in thermal axial stress  
505 and thermal axial displacement were evaluated using the results from a series of physical  
506 modeling experiments on centrifuge-scale energy foundations in dry sand and unsaturated silt  
507 layers. Specifically, the effects of end-bearing and semi-floating boundary conditions at the  
508 foundation toe and free-expansion and restrained-expansion boundary conditions at the  
509 foundation head were considered. The following specific conclusions can be drawn from the  
510 results:

- 511 • The thermal axial stresses were greater for energy foundations in compacted silt than in dry  
512 sand. This was attributed to greater soil-structure interaction due to the greater initial radial  
513 stresses in the compacted silt.
- 514 • The thermal axial stresses were greater for end-bearing energy foundations than semi-  
515 floating foundations due to the restraint provided by the rigid bottom boundary condition.
- 516 • An increase in thermal axial stress of nearly 100% was observed in the case where the head  
517 of an end-bearing foundation in dry sand was restrained than when it was permitted to  
518 expand upward freely.
- 519 • The results from the semi-floating foundations provide new insight into the potential  
520 behavior of energy foundations that obtain their axial capacity primarily through skin  
521 friction. The slope of the displacement curves were observed to consistently flatten with  
522 increasing temperature. Although a downward movement in the null point associated with  
523 increased restraint was expected with increasing temperature, inconsistent trends were  
524 observed in the data. An upward shift in the null point was observed in the foundations in silt  
525 potentially due to greater thermally-induced drying of the unsaturated silt around the head of



526 the foundation. Overall, the results indicate that only slight movements in the null point for  
527 semi-floating energy foundations are expected.

528 • Heating of semi-floating energy foundations in compacted silt was observed to lead to a clear  
529 increase in the ultimate capacity, but it led to a negligible effect for semi-floating energy  
530 foundations in sand. This was proposed to be due to a combination of radial stress changes  
531 and thermally-induced water flow in the unsaturated soil. The initial lateral stresses in the silt  
532 and sand differed due to different the preparation techniques, and a greater amount of  
533 differential radial thermal expansion may have occurred for the foundation in the silt due to  
534 the higher lateral stresses induced by compaction. Thermally-induced water flow away from  
535 the foundation is only expected in unsaturated soils, but will lead to an increase in effective  
536 stress on the soil-foundation interface. These effects are complex, and deserve simulation  
537 using coupled flow-deformation models that consider differential expansion of the  
538 foundation and soil.

## 539 **ACKNOWLEDGMENTS**

540 The authors would like to thank Dr. Min Zhang for her assistance in the centrifuge testing.  
541 Financial support from NSF grant CMMI-0928159 is gratefully acknowledged. The contents of  
542 this paper reflect the views of the authors and do not necessarily reflect the views of the sponsor.

543 **APPENDIX I. REFERENCES**

- 544 Amatya, B.L., Soga, K., Bourne-Webb, P.J., Amis, T., and Laloui, L. (2012). “Thermo-  
545 mechanical behaviour of energy piles.” *Géotechnique*. 62(6), 503–519.
- 546 Akrouch, G., Sanchez, M., Briaud, J.-L. (2014). “Thermo-mechanical behavior of energy piles in  
547 high plasticity clays.” *Acta Geotechnica*. 9(3), 399-412.
- 548 Bouazza, A., Singh, R.M., Wang, B., Barry-Macaulay, D., Haberfield, C., Chapman, G.,  
549 Baycan, S., and Carden, Y. (2011). “Harnessing on site renewable energy through pile  
550 foundations.” *Australian Geomechanics*. 46(4), 79-90.
- 551 Bourne-Webb, P.J., Amatya, B., Soga, K., Amis, T., Davidson, C. and Payne, P. (2009). “Energy  
552 pile test at Lambeth College, London: Geotechnical and thermodynamic aspects of pile  
553 response to heat cycles.” *Géotechnique*. 59(3), 237–248.
- 554 Brandl, H. (1998). “Energy piles and diaphragm walls for heat transfer from and into the  
555 ground.” *Proceedings of the 3<sup>rd</sup> International Geotechnical Seminar on Deep Foundations  
556 on Bored and Auger Piles, BAP III, Ghent, Belgium. October 19-21. Balkema,  
557 Rotterdam. 37–60.*
- 558 Brandl, H. (2006). “Energy foundations and other thermo-active ground structures.”  
559 *Géotechnique*. 56(2), 81-122.
- 560 Davisson, M.T. (1973). “High capacity piles.” “*Innovation in Foundations Construction.*” *Soil  
561 Mech. Div., Illinois Section, ASCE, Chicago, Ill., pp. 81-112.*
- 562 Goode, J.C., III. (2013). *Centrifuge Modeling of the Thermo-Mechanical Response of Energy  
563 Foundations. MS Thesis. University of Colorado Boulder. 221 pg.*
- 564 Goode, J.C., III, Zhang, M. and McCartney, J.S. (2014). “Centrifuge modeling of energy  
565 foundations in sand.” *Proc. 8<sup>th</sup> International Conference on Physical Modelling in*

566 Geotechnics (ICPMG 2014). Perth, Australia. January 14-17, 2014. CRC Press. pg. 729-  
567 736.

568 Goode, J.C., III and McCartney, J.S. (2014). "Evaluation of head restraint effects on energy  
569 foundations." Proceedings of GeoCongress 2014 (GSP 234), M. Abu-Farsakh and L.  
570 Hoyos, eds. ASCE. 2685-2694.

571 Knellwolf, C., Peron, H., and Laloui, L. (2011). "Geotechnical analysis of heat exchanger piles."  
572 ASCE Journal of Geotechnical and Geoenvironmental Engineering. 137(12), 890-902.

573 Laloui, L., Moreni, M. and Vulliet, L. (2003). "Comportement d'un pieu bi-fonction, foundation  
574 et échangeur de chaleur." Canadian Geotechnical Journal. 40(2), 388-402.

575 Laloui, L., Nuth, M. and Vulliet, L. (2006). "Experimental and numerical investigations of the  
576 behaviour of a heat exchanger pile." International Journal of Numerical and Analytical  
577 Methods in Geomechanics. 30(8), 763-781.

578 McCartney, J.S. and Rosenberg, J.E. (2011). "Impact of heat exchange on side shear in thermo-  
579 active foundations." Proc. Geo-Frontiers 2011 (GSP 211). J. Han and D.E. Alzamora,  
580 eds. ASCE, Reston VA. pg. 488-498.

581 McCartney, J.S. and Murphy, K.D. (2012). "Strain distributions in full-scale energy  
582 foundations." DFI Journal. 6(2), 28-36.

583 Mimouni T. and Laloui L. (2014). "Towards a secure basis for the design of geothermal piles."  
584 Acta Geotechnica. 9(3), 355-366. DOI 10.1007/s11440-013-0245-4.

585 Murphy, K.D., McCartney, J.S., Henry, K.H. (2014). "Thermo-mechanical response tests on  
586 energy foundations with different heat exchanger configurations." Acta Geotechnica. 1-  
587 17. DOI: 10.1007/s11440-013-0298-4.

588 Murphy, K.D. and McCartney, J.S. (2014). “Seasonal response of energy foundations during  
589 building operation.” *Geotechnical and Geological Engineering*. 1-14. DOI:  
590 10.1007/s10706-014-9802-3.

591 Olgun, C.G., Ozudogru, T., and Arson, C.F. (2014). “Thermo-mechanical radial expansion of  
592 heat exchanger piles and possible effects on contact pressures at pile–soil interface.”  
593 *Géotechnique Letters*. 4(3) 170-178.

594 Ouyang Y., Soga K. and Leung Y.F. (2011). “Numerical back-analysis of energy pile test at  
595 Lambeth College, London.” *Proc. Geo-Frontiers 2011 (GSP 211)*. J. Han and D.E.  
596 Alzamora, eds. ASCE, Reston VA. pg. 440-449.

597 Suryatriyastuti, M.E., Mroueh, H., and Burlon, S. (2013). “Chapter 7: Numerical analysis of the  
598 bearing capacity of thermoactive piles under cyclic axial loading.” *Energy Geotechniques*.  
599 L. Laloui and A. DiDonna, eds. John Wiley and Sons. London.

600 Stewart, M.A. and McCartney, J.S. (2014). “Centrifuge modeling of soil-structure interaction in  
601 energy foundations.” *ASCE Journal of Geotechnical and Geoenvironmental Engineering*.  
602 140(4), 04013044-1-11. DOI: 10.1061/(ASCE)GT.1943-5606.0001061.

603 Sutman, M., Brettmann, T., and Olgun, C.G., 2014. Thermo-mechanical behavior of energy  
604 piles: Full-scale field test verification. DFI 39th Annual Conference on Deep  
605 Foundations, Atlanta, GA. Oct. 21-24. pg. 1-11. (CD-ROM).

606 Wang, W., Regueiro, R., Stewart, M.A., and McCartney, J.S. (2012). “Coupled thermo-poro-  
607 mechanical finite element analysis of a heated single pile centrifuge experiment in  
608 saturated silt.” *Proc., GeoCongress 2012 (GSP 225)*, R. D. Hryciw, A. Athanasopoulos-  
609 Zekkos, and N. Yesiller, eds., ASCE, Reston, VA. pg. 4406-4415.

610 Wang, B., Bouazza, A., Singh, R., Haberfield, C., Barry-Macaulay, D., and Baycan, S. (2014a).  
611 “Post-temperature effects on shaft capacity of a full-scale geothermal energy pile.” J.  
612 Geotech. Geoenviron. Eng., 10.1061/(ASCE)GT.1943-5606.0001266, 04014125.

613 Wang, W., Regueiro, R. and McCartney, J.S. (2014b). “Coupled Axisymmetric Thermo-Poro-  
614 Elasto-Plastic Finite Element Analysis of Energy Foundation Centrifuge Experiments in  
615 Partially Saturated Silt.” Geotechnical and Geological Engineering. 1-16. DOI:  
616 10.1007/s10706-014-9801-4.

617

618 **LIST OF TABLE AND FIGURE CAPTIONS**

619 **Table 1:** Properties of Nevada sand and Bonny Silt used in the different experiments

620 **Table 2:** Details of centrifuge tests on semi-floating (short) and end-bearing (long) foundations

621 **Fig. 1.** Schematics of the scale model energy foundations including locations of the embedded  
622 strain gages and thermocouples

623 **Fig. 2.** Typical strain gage calibration results: (a) Individual gage correction before embedment;  
624 (b) Axial strain measurements in the long foundation after mechanical correction;  
625 (c) Thermal axial strain measurements in the long foundation after thermal correction

626 **Fig. 3.** Locations of instrumentation in the energy foundation tests

627 **Fig. 4.** Results from tests on semi-floating foundations in Nevada sand: (a, b, c, d) Load and  
628 displacement in Tests 1, 2, 3, 4; (e, f, g, h) Foundation temperatures in Tests 1, 2, 3, 4;  
629 (i, j, k, l) Axial strains in Tests 1, 2, 3, 4

630 **Fig. 5.** Results from tests on semi-floating foundations in Bonny silt: (a, b, c) Load and  
631 displacement for Tests 5, 6, 7; (d, e, f) Foundation temperatures for Tests 5, 6, 7; (g, h, i)  
632 Axial strains for Tests 5, 6, 7

633 **Fig. 6.** Results from tests on end-bearing foundations in Nevada sand: (a, b) Load and  
634 displacement in Tests 8 and 9; (c, d) Foundation temperatures in Tests 8 and 9; (e, f)  
635 Axial strains in Tests 8 and 9

636 **Fig. 7.** Results from a test on an end-bearing foundation in Bonny silt (Test 10): (a) Load and  
637 displacement; (b) Foundation temperatures; (c) Axial strains

638 **Fig. 8.** Synthesis of thermo-mechanical behavior of semi-floating foundations in Nevada sand  
639 (Tests 2-4): (a) Temperature profiles; (b) Thermal axial strain profiles; (c) Thermal axial  
640 stress profiles; (d) Thermal axial displacement profiles

641 **Fig. 9.** Synthesis of thermo-mechanical behavior of semi-floating foundations in Bonny silt  
642 (Tests 6 and 7): (a) Temperature profiles; (b) Thermal axial strain profiles; (c) Thermal  
643 axial stress profiles; (d) Thermal axial displacement profiles

644 **Fig. 10.** Summary of load-displacement curves for semi-floating energy foundations under  
645 different temperatures (a) Nevada sand (Tests 1-4); (b) Bonny silt (Test 5-7)

646 **Fig. 11.** Synthesis of thermo-mechanical behavior of end-bearing foundations in Nevada sand  
647 (Tests 8 and 9): (a) Temperature profiles; (b) Thermal axial strain profiles; (c) Thermal  
648 axial stress profiles; (d) Thermal axial displacement profiles

649 **Fig. 12.** Synthesis of thermo-mechanical behavior of an end-bearing foundation in Bonny silt in  
650 Test 10 (open symbols: before loading; closed symbols: after loading): (a) Temperature  
651 profiles; (b) Thermal axial strain profiles; (c) Thermal axial stress profiles; (d) Thermal  
652 axial displacement profiles

653 **Fig. 13.** Load-settlement behavior of end-bearing foundations in different soil layers: (a) Nevada  
654 Sand (Tests 8 and 9); (b) Bonny silt (Test 10)

655

656 **Table 1:** Properties of Nevada sand and Bonny silt used in the different experiments

Parameter	Nevada Sand	Bonny Silt
D <sub>10</sub>	0.09 mm	< 0.0013 mm
D <sub>30</sub>	0.11 mm	0.022 mm
D <sub>50</sub>	0.16 mm	0.039 mm
% Passing No. 200 Sieve	0	83.9 %
% Clay Size	0	14.0 %
% Silt Size	0	69.9 %
% Sand Size	100	16.1 %
G <sub>s</sub>	2.65	2.6
Liquid Limit, LL	-	25
Plastic Limit, PL	-	21
Plasticity Index, PI	-	4
Activity, A	-	0.29
Effective friction angle, $\phi$	35°	32.4°
Compression index, C <sub>c</sub>	-	0.015
Recompression index, C <sub>r</sub>	-	0.0017
Std. Proctor Max. Dry Unit Weight	-	16.9 kN/m <sup>3</sup>
Std. Proctor Max. Opt. Water Content	-	13.6%
Initial void ratio, e <sub>0</sub>	0.75	0.63
Initial water content, w <sub>0</sub>	0	14.2%
Initial degree of saturation, S <sub>0</sub>	0	0.59
Saturated hydraulic conductivity, k <sub>s</sub>	1.0 × 10 <sup>-4</sup> m/s	7.6 × 10 <sup>-8</sup> m/s
Thermal conductivity for e <sub>0</sub> and S <sub>0</sub> , $\lambda$	0.25	1.147 W/mK

657

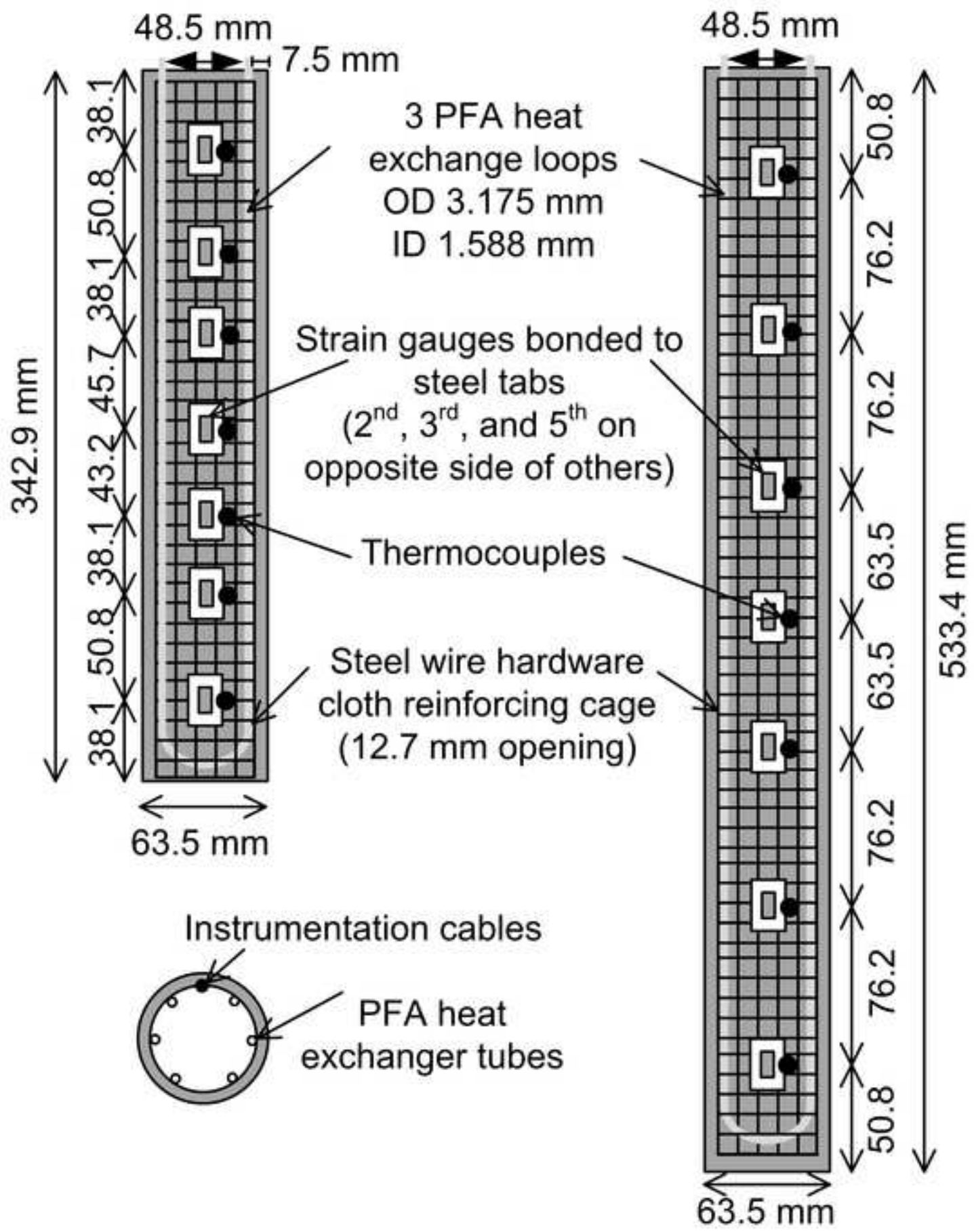


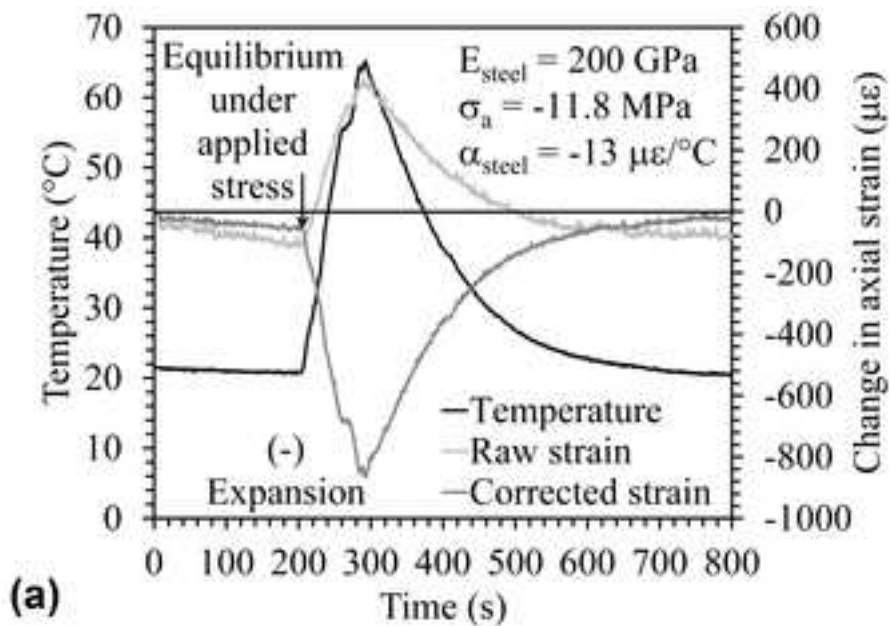
658 **Table 2:** Details of centrifuge tests on semi-floating (short) and end-bearing (long) foundations

659 (Note: All tests performed at a g-level of 24)

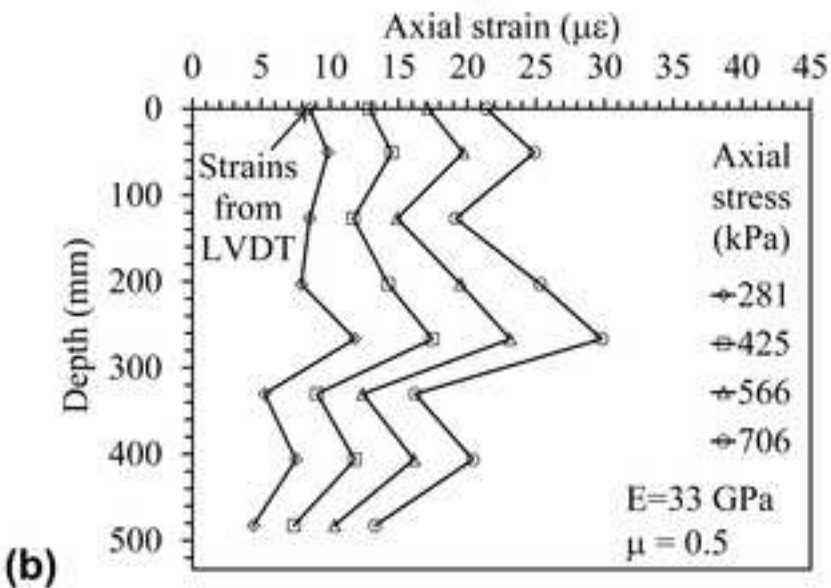
Test	Soil	Foundation	Load or Stiffness Control	Soil Total Unit Weight	Comp. Water Content	Thermal Conductivity	T <sub>ave</sub> at Loading to Failure	ΔT <sub>ave</sub> at Loading to Failure
				(kN/m <sup>3</sup> )	(%)	W/(mK)	(°C)	(°C)
1	Nevada	Short	Load	15.5	-	-	23.0	0.0
2	Nevada	Short	Load	15.5	-	-	30.2	7.0
3	Nevada	Short	Load	15.5	-	0.265	35.3	12.0
4	Nevada	Short	Load	15.5	-	-	40.3	18.0
5	Bonny	Short	Load	17.0	12.3	1.234	21.4	0.0
6	Bonny	Short	Load	17.0	12.6	1.237	30.5	10.0
7	Bonny	Short	Load	17.0	12.5	1.252	38.0	18.0
8	Nevada	Long	Load	15.5	-	-	33.4	11.1
9	Nevada	Long	Stiffness	15.5	-	-	33.3	11.8
10	Bonny	Long	Load	17.0	12.2	1.150	21.6, 31.1, 36.3, 37.5, 27.7	0.0, 9.5, 14.7, 15.9, 6.1

660

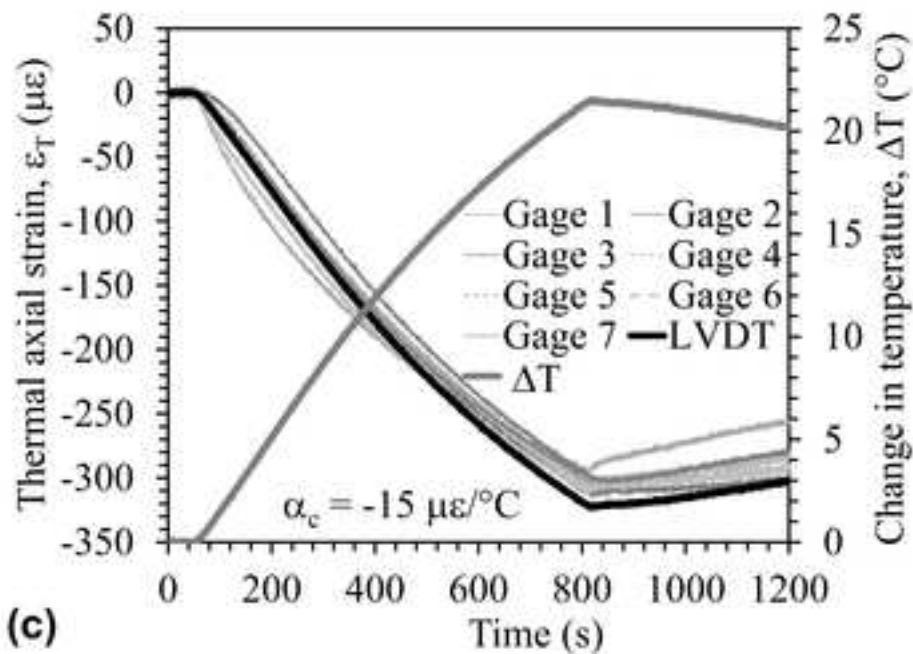




(a)



(b)



(c)

